Scripta Materialia 251 (2024) 116206

Contents lists available at ScienceDirect

Scripta Materialia

journal homepage: www.journals.elsevier.com/scripta-materialia

Viewpoint article

# Opportunities for novel refractory alloy thermal/environmental barrier coatings using multicomponent rare earth oxides

Kristyn D. Ardrey [a,*], Mackenzie J. Ridley [a], Kang Wang [a], Kevin Reuwer [d], Giavanna Angelo [d], Kevin Childrey [e], William Riffe [a], Mahboobe Jassas [b], Mukil Ayyasamy [a], Prasanna V. Balachandran [a,b], Patrick E. Hopkins [a,b,c], Jonathan Laurer [e], Carolina Tallon [d], Bi-Cheng Zhou [a], Elizabeth J. Opila [a,b]

[a] Departments of Materials Science and Engineering, University of Virginia, Charlottesville, VA 22904, USA
[b] Department of Mechanical and Aerospace Engineering, University of Virginia, Charlottesville, VA 22904, USA
[c] Department of Physics, University of Virginia, Charlottesville, VA 22904, USA
[d] Department of Materials Science and Engineering, Virginia Polytechnic Institute and State University, Blacksburg, VA 24061, USA
[e] Commonwealth Center of Advance Manufacturing, Disputanta, VA 23842, USA

ARTICLE INFO

*Keywords:*
Thermal barrier coating
Protective coating
Refractory metals
Rare Earth
Oxide

ABSTRACT

Opportunities are described for developing coatings for refractory alloys beyond the current state-of-the-art silicide coatings, which are inadequate for long-term application in combustion environments due to silica volatility. It is proposed that multicomponent rare earth oxides provide an ideal material system to tailor all necessary properties for environmental/thermal barrier coatings in a single layer, differing from current trends to adopt multi-layer systems that are prone to thermochemical-mechanical interface failure mechanisms. The article discusses opportunities, proof-of-concept, and challenges to accomplish these single-layer rare earth oxide coatings. Properties of interest include isotropic phase stability, processability, thermal expansion, thermal conductivity, ability to perform as a radiation barrier, stability in combustion environments, CMAS resistance, and ability to act as an oxygen diffusion barrier. Both experimental and computational approaches for property optimization are described.

## Introduction

Brayton cycle aeroturbine engines increase in efficiency as the operating temperatures are increased. Ni-base superalloys with thermal barrier coatings (TBCs) have enabled high temperature efficient aeroturbine engines, however, the superalloy/TBC system has reached its upper use temperature limit. Yttria-stabilized zirconia (YSZ) and gadolinium zirconate (GZO) TBCs have been engineered through microstructural control during processing to incorporate porosity and boundaries. In combination with the low intrinsic thermal conductivity of the coating materials and backside cooling of the metallic component, these systems can achieve significant temperature drops from the hot gas surface to the underlying metallic bond coat, reducing metallic surface temperatures. However, further significant improvements in the superalloy/TBC systems are unlikely. Rare earth silicate environmental barrier coatings (EBCs) on SiC-based ceramic matrix composites (CMCs) offer opportunities to achieve higher engine operating temperatures and reduced use of backside cooling air, but current EBC/CMC systems are limited by the melting temperature of the silicon bond coat (1414 °C). Refractory metal alloys (RMAs) offer a third materials option to increase operating temperatures of aeroturbine engines, however, these alloys based on group IV, V, and VI metals suffer from rapid degradation in oxidizing environments. Thus, prime reliant environmental barrier coatings must be used for refractory alloy implementation in aeroturbine engines. State-of-the-art coatings for Nb-base alloys are metal silicides that react in oxidizing environments to form silica [1,2], which may or may not have an oxide topcoat. However, thermally grown silica has been shown to be inadequate for long-term hot section turbine engine applications [3]. The proposed oxide topcoats (YSZ, $Gd_2Zr_2O_7$) are not oxygen barriers and require NiCrAlY or silicide bond coats [4,5]. Furthermore, coating system validation in high temperature water vapor is critical for barriers based on $SiO_2$ since it is known to be volatile in

* Corresponding author.
*E-mail address:* kdardrey@gmail.com (K.D. Ardrey).

https://doi.org/10.1016/j.scriptamat.2024.116206
Received 26 December 2023; Received in revised form 18 May 2024; Accepted 26 May 2024
Available online 4 June 2024

water vapor [6,7].

Further performance gains for refractory alloy hot section turbine components can be enabled if the EBCs are also thermal barriers, i.e. T/EBCs, assuming backside component cooling. In this work we illustrate that multicomponent rare-earth oxides (MRO) enable the design of coating properties to meet multiple requirements for optimization of the RMA/coating system performance. Rare earth oxides, $RE_2O_3$, have been considered for $Al_2O_3$-based ceramic composites [8], yet they have not yet been considered for RMA applications. Furthermore, the sixteen rare earths (the lanthanides plus scandium and yttrium, minus the unstable promethium) as sesquioxides offer promise for co-optimization of coating phase stability, thermal expansion match to RMAs, chemical stability of the RMA/MRO interface, coating thermochemical stability in combustion gases, resistance to molten deposit degradation, reduced oxidant permeability to mitigate poor oxidation resistance of RMAs, reduced coating thermal conductivity, and the potential for reduced radiation heat fluxes through the coating. MRO coatings can be fabricated by standard atmospheric plasma spray and slurry coating processing methods, demonstrating manufacturability. We describe the promise of using MROs for each property and identify challenges to implement single layer MRO coatings on commercially available C-103 Nb-base alloys as proof of concept for further development on other more oxidation resistant RMAs. A schematic of the MRO coating concept for RMAs can be seen in Fig. 1.

### *MRO composition selection and phase stability*

The criteria for MRO composition selection has three main components: First, multiple RE cations of varying size and mass in $RE_2O_3$ are desired to increase phonon scattering and reduce the coating thermal conductivity [9–11]. Second, a cubic phase is desired to reduce stresses due to anisotropic thermal expansion upon cooling. Third, we choose $Y_2O_3$ as the cubic phase base material due to its lower cost and mass relative to the other $RE_2O_3$. Additional $RE_2O_3$ components are selected to optimize coating properties as described throughout the paper. Fig. 2 **(a)** shows that the smaller RE cations form cubic polymorphs of $RE_2O_3$, whereas monoclinic and hexagonal polymorphs are formed for the larger RE cations. Fig. 2**(b)** shows the solubility of $RE_2O_3$ in $Y_2O_3$ as determined by CALPHAD modeling, demonstrating that as RE cation size increases, the solubility in the cubic $Y_2O_3$ decreases. The solubility limits are determined from the phase boundaries between cubic $Y_2O_3$ with other phases, where the solubility for La is from Chen et al. [12] and the rest are calculated using the thermodynamic data from Zinkevich [13]. Nevertheless, significant solubility of even $La_2O_3$ (La being the largest cation) exists, allowing selection of an assemblage of RE cations to optimize sometimes competing properties. Challenges to identify the optimum mix are being addressed via machine learning models [14], which so far have focused on equimolar compositions. Optimization can likely be obtained via off-equimolar compositions resulting in cost savings by usage of more abundant $RE_2O_3$ [15] such as $Y_2O_3$. However, no work has yet addressed this challenge.

The MRO coating must be stable with underlying alloys, i.e. the alloy cannot have a more stable oxide than $RE_2O_3$. According to Zinkevich [13], the standard enthalpy of formation of $RE_2O_3$ range between −1288 kJ/mol for $Y_2O_3$ and −1110 kJ/mol $O_2$ for $Eu_2O_3$. In contrast, the enthalpy of formation of $Nb_2O_5$ is -760 kJ/mol $O_2$. Thus, any $RE_2O_3$ should be stable in contact with Nb, and many are even stable in contact with Hf, with an enthalpy of formation of $HfO_2$ of −1145 kJ/mol $O_2$. This is further borne out by the Nb-Y-O ternary phase diagram [16], showing no intermediate phase formation on the tie line between Nb and $Y_2O_3$. A critical assessment of the RMA/MRO interface stability is needed for other RMAs that contain group IV metals more likely to getter oxygen.

### *Synthesis and application of free-standing and multicomponent $RE_2O_3$ coatings*

Free-standing MRO compositions were synthesized to demonstrate our ability to tailor multiple properties of this class of materials. Powders of single component $RE_2O_3$ (RE = Nd, Yb, Y, Er, Ho) (Linde Advance Material Technologies, Indianapolis, IN) $La_2O_3$ (Elemental Metals, Randolph, NJ) and a pre-reacted ternary $(Y_{0.33}Yb_{0.33}Er_{0.33})_2O_3$ (Oerlikon Metco, Westbury, NY) were utilized for both free-standing coupons and coated Nb-base alloy substrates. Selected mixtures were fabricated into coupons via spark plasma sintering (SPS) (65 MPa, 1700 °C) to achieve a homogenous solid solution by thermal diffusion. SPS coupons of MRO mixtures were used for linear coefficient of thermal expansion (CTE) characterization, thermal conductivity testing, and thermochemical analysis.

Coating fabricability is a clear need for any new material system. Two manufacturing approaches for MRO coatings were demonstrated: i) *atmospheric plasma spraying (APS)*, the current industrial standard technology for ceramic coatings; and ii)*slurry coating*, an approach for tailoring coating properties, enabling microstructure control, and allowing for potential cost reduction and repairability.

Although there is a body of scientific work for both routes in the

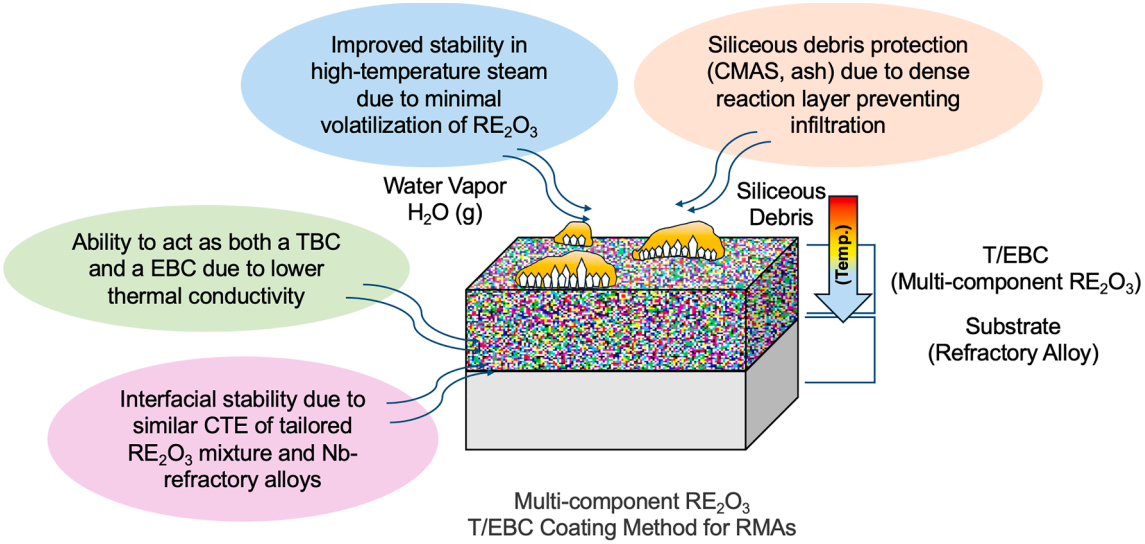


**Fig. 1.** Single layer T/EBC multicomponent $RE_2O_3$ coating for RMAs.

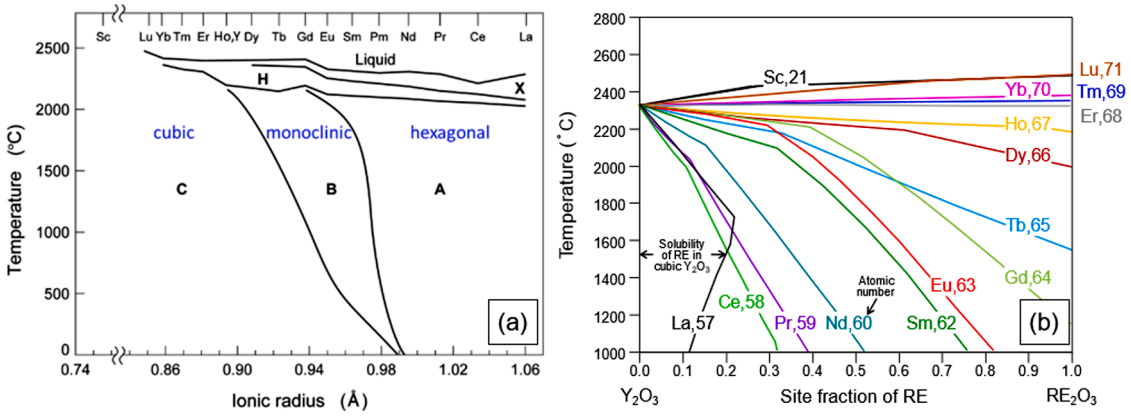


**Fig. 2.** (a) Polymorphs of $RE_2O_3$ (reproduced from Zinkevich); (b) Calculated solubility limits of $RE_2O_3$ in $Y_2O_3$.

literature for oxide ceramic materials in terms of potential parameter values, mechanism of deposition, and role of microstructure in performance [17–26], there are no data available for multicomponent rare earth oxides. A side-by-side comparison between both manufacturing technologies was implemented to explore the role of processing in the microstructure and properties of the MRO coatings and to advance the science behind manufacturing coatings with these materials and formulations. Multiple three-component MRO materials were evaluated with increasing amounts of least costly $Y_2O_3$ to investigate property trade-off with unit affordability, as shown in Table 1.

The APS and slurry manufacturing technologies described here require very distinct types of particle sizes and distributions: spherical larger granules for APS, and individual particles below 1 μm size for the slurry process, with narrow size distributions. The three-component compositions used in this study were sourced from Oerlikon-Metco (Westbury, NY) with the same chemical purity but in two distinctive size ranges, suitable for each of the manufacturing routes, in large batches of 5–10 kg for each composition. Each composition was confirmed by X-ray diffraction (XRD) analysis of the raw materials to be single phase cubic demonstrating feasibility of MRO powder production. Thick coatings (100–400 μm) of rare earth oxide blends containing yttrium, erbium, and ytterbium oxides were successfully applied to C-103 alloy substrates via APS. Average coating thicknesses measured at ~400 μm and 170 μm were produced, showing good substrate adhesion and uniformly distributed porosity within the coating. However, depositing crack-free APS coatings at small radius features remains a challenge.

MRO slurry suspensions were optimized for solid particle loading, use of a water solvent, dispersants, binders, pH and sintering schedule to achieve high-density coatings. Formulations containing 30 to 50 vol% solid content in deionized water with 1 wt.% dispersant at a pH of 10 were utilized to enable a stable suspension via controlled interparticle forces and suitable viscosity to minimize drying stresses [27]. The equimolar 3-component $RE_2O_3$ powder has an isoelectric point (IEP) of 4, that is slightly higher than reported in the literature for $Y_2O_3$, the major component of the formulation (IEP 2.5) [28] and a maximum zeta potential (ζ) around −20 mV indicating that under these pH conditions, a stable suspension can be achieved. The suspensions were slip-cast into free-standing pellets and sintered at 1600 °C/2.5 h, rendering a sintered density of 97 %, confirming that the solid content and suspension formulation translates to a good green particle packing and sintered density.

**Table 1**
Selected three-component MRO formulations for processing study.

| | $Y_2O_3$ (%mol) | $Er_2O_3$ (%mol) | $Yb_2O_3$ (%mol) |
|---|---|---|---|
| **Composition 1** | 60 | 20 | 20 |
| **Composition 2** | 50 | 30 | 20 |
| **Composition 3** | 34 | 33 | 33 |

The advantages of the slurry synthesis routes relative to APS are possibilities for *i)* use of a binder to create a network that will "hold in place" the particulates in the coating; *ii)* higher particle packing that will translate into higher strength, more homogeneity and less defects; *iii)* minimization of cracking, delamination or defects that typically arise from the capillary pressures associated with drying and removal of solvent, especially when the thickness of the coating increases; i*v)* shorter consolidation times, *v)* suitability for coating repairs in complex shapes and difficult-to-access sections of the samples (non-line-of-sight) and; *vi)* possibility of developing mixed phases, multi-layer, porous and or compositionally graded coatings for higher thermal stability and control of the fracture toughness.

*Tailoring thermal properties*

**Thermal Expansion:** An excellent thermal expansion match between the alloy substrate [29] and the coating is key to coating adherence. Fig. 3**(a)** displays an MRO composition plotted alongside CTE analysis of single component RE oxides included in the composition. Even with additions of hexagonal $Nd_2O_3$, an isotropic cubic CTE behavior is maintained. Fig. 3**(b)** displays the thermal expansion coefficients of several MRO compositions compared to C-103. The difference in CTE will result in stresses generated at the interface and throughout the coating. However, coating microstructure design is expected to enable CTE differences up to about 2 ppm/ °C [30]. Furthermore, the CTEs of other RMA, for example the Senkov alloy [31], are expected to be higher with group IV metal additions (~9 ppm/ °C for Hf and Zr) compared to that of Nb-base alloys (~7.5 ppm/ °C for C-103) [30]. Thus, the ability to tailor CTE of MRO to a variety of RMA compositions is an example of property optimization via $RE_2O_3$ compositional selection.

**Thermal Conductivity:** Thermal conductivity is a key design consideration for T/EBCs. Materials with a lower thermal conductivity when coupled with backside cooling enable lower RMA surface temperatures thereby limiting thermomechanical and thermochemical-driven failure mechanisms [32]. By design, high entropy and entropy stabilized oxides exhibit remarkably low thermal conductivities due to increased phonon scattering mechanisms arising from the relatively large solubility and distribution of different types of cations in the ceramic [33–38]. This variety of masses and atomic radii can result in ultralow thermal conductivities of multicomponent oxides [9], exceeding even those of their respective amorphous phases and theoretical minimum limits [35,39]. These concepts have been previously identified as mechanisms to reduce thermal conductivity of environmental barrier coatings [40,41]. The key to achieving further reduction

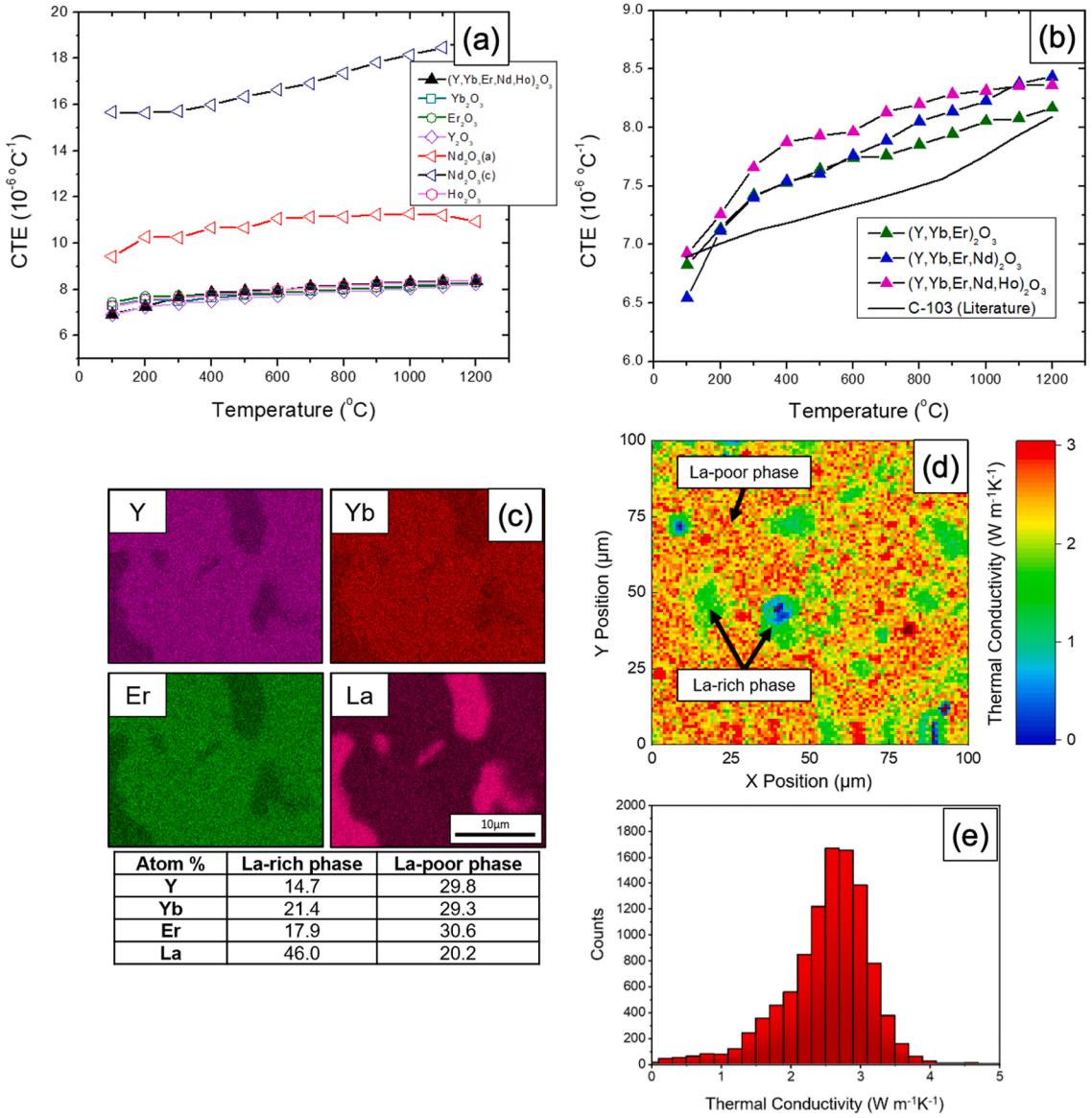


| Atom % | La-rich phase | La-poor phase |
|---|---|---|
| Y | 14.7 | 29.8 |
| Yb | 21.4 | 29.3 |
| Er | 17.9 | 30.6 |
| La | 46.0 | 20.2 |

**Fig. 3.** CTE of five component MRO $(Y_{0.2}Yb_{0.2}Er_{0.2}Ho_{0.2}Nd_{0.2})_2O_3$ along-side CTE analysis of each $RE_2O_3$ within the composition; (b) CTE of C-103 compared to MRO compositions with 3, 4, and 5 components. All thermal expansion results for individual $RE_2O_3$ and MRO compositions were acquired via hot-stage X-ray diffraction of samples in powder form from lattice spacing analysis via Rietveld refinement (GSAS II) with a weighted profile R-factor ($R_{wp}$) of ~ 7%–12%; (c) EDS maps for RE in $(Y_{0.28}Yb_{0.28}Er_{0.28}La_{0.16})_2O_3$ sample phases; (c) Thermal conductivity maps of a different region in this sample; (d) Histogram of the measured thermal conductivities in (e).

in thermal conductivities is introducing additional phonon scattering mechanisms beyond mass scattering alone, such as local lattice distortions or nanoscale grain or phase boundaries, as discussed in our prior works [34,42].

The room temperature thermal conductivity of individual and multicomponent $RE_2O_3$ fabricated by SPS are shown in Table 2. First, the thermal conductivity of the $Y_2O_3$ sample is lower than that of a single crystal [43] due to polycrystallinity; this is not surprising since even the addition of even 1 mole% of Nd in $Y_2O_3$ can lead to a factor of two reduction in thermal conductivity [44]. Single component $Nd_2O_3$ has an anisotropic hexagonal crystal structure rendering its thermal conductivity lower than isotropic cubic structures. The three- and five-cation solid solution cubic $RE_2O_3$ compositions have similar thermal conductivities only slightly lower than that of the $Nd_2O_3$ sample. The $(Y_{0.28}Yb_{0.28}Er_{0.28}La_{0.16})_2O_3$ composition has a $La_2O_3$ content above the solubility limit and thus forms two phases, shown in Fig. 3**(c)**. This two-phase composition's thermal conductivity is reduced as compared to all other samples, including the cubic MRO composition, which we attribute to the influence of the second phase introducing additional scattering mechanisms beyond phonon-phonon and phonon-mass impurity scattering alone. Here we emphasize that the crystal structure and phase content are important contributors to reducing the thermal

**Table 2**
Room temperature thermal conductivity of the RE-oxides and selected MRO compositions.

| MRO composition | Crystal Structure | Thermal Conductivity ($Wm^{-1}K^{-1}$) |
|---|---|---|
| $Y_2O_3$ | cubic | 10.0 ± 0.9 |
| $Nd_2O_3$ | hexagonal | 3.8 ± 0.5 |
| $(Y_{0.33}Yb_{0.33}Er_{0.33})_2O_3$ | cubic | 3.3 ± 0.4 |
| $(Y_{0.2}Yb_{0.2}Er_{0.2}Ho_{0.2}Nd_{0.2})_2O_3$ | cubic | 3.2 ± 0.4 |
| $(Y_{0.28}Yb_{0.28}Er_{0.28}La_{0.16})_2O_3$ | cubic + orthorhombic | 2.7 ± 0.4 |

conductivity in addition to multiple cations of varying mass and size.

The thermal conductivities reported in Table 2 are at room temperature. In general, the thermal conductivities of complex oxides with multiple cations (including high entropy) remain relatively constant as a function of temperature. This is due to the fact that the multiple different atoms with different masses in the crystal lead to increased phonon scattering that is temperature independent [9]. In monatomic single crystals, the thermal conductivity decreases as a function of temperature due to anharmonic phonon scattering (i.e., Umklapp processes) [45]. When additional cations are included in mixed atom crystals or solid solutions, the lattice sites that are occupied by different atoms serve to scatter phonons based on changes in cation mass, radius and changes in the local bonding environment. This constant thermal conductivity with increased temperature has been shown for various multiple-component rare earth oxides and high entropy oxides [34]. Thus, we expect the reported room temperature thermal conductivities of the multi-cation rare earth oxides to be similar to their high temperature values.

We performed spatially resolved thermal conductivity measurements of the $(Y_{0.28}Yb_{0.28}Er_{0.28}La_{0.16})_2O_3$ composition with areal resolution on the order of ~2 micrometers using time domain thermoreflectance (TDTR) [46–48], the same method used to acquire average results reported in Table 2. Details of this technique have been previously described [49–52], including a recent review [53]. A thermal conductivity map of the $(Y_{0.28}Yb_{0.28}Er_{0.28}La_{0.16})_2O_3$ sample is shown in Fig. 3 **(d)**. Two distinct thermal conductivities are observed, the higher of which we attribute to the cubic solution phase and the lower of which is due to the second $La_2O_3$-rich phase. A histogram of the thermal conductivity values in the thermal conductivity map is shown in Fig. 3**(e)**. The modes of these thermal conductivity distributions correspond to the average thermal conductivities of $(Y_{0.28}Yb_{0.28}Er_{0.28}La_{0.16})_2O_3$ reported in Table 2 collected from TDTR measurements on this sample with larger pump and probe spot sizes and thus coarser spatial resolution. Importantly, the $La_2O_3$-rich phase has ultralow thermal conductivity with values similar to the predicted lower limit to thermal conductivity [39] of cubic RE oxides, ~1.3 W $m^{-1}$ $K^{-1}$ for $Y_2O_3$. Nanoscopic phonon scattering mechanisms that lead to these ultralow thermal conductivities in the presence of RE oxide second phases, the role that these second phases and their length scale have on phonon scattering and thermal conductivity of composites are important scientific questions to further pursue to enable additional reductions in thermal conductivity of MRO coatings.

While the low thermal conductivities of these MRO coatings offer promise as thermally protective coatings by reducing heat conduction, at engine relevant temperatures black body emission at 1 – 4 μm from the hot gas and surfaces can lead to radiative heating of the turbine blade [54]. This radiative energy transmits through most oxides of interest as T/EBCs. In 2019, Flament and Clarke [54] proposed the concept of a radiative barrier coating by utilizing the strong near-IR absorption bands of rare earth oxides, which have peaks in their absorption spectrum in this spectral range of interest [55]. Thus, a potential added benefit of our MRO coatings is the ability to serve as radiation barriers. The high temperature optical and radiative properties of these systems are yet to be critically assessed and are an active area of research.

### *Tailoring thermochemical stability in reactive environments*

**High Temperature Steam Exposure Stability:** Environmental barrier coatings must withstand high temperature combustion gases, specifically high-velocity water vapor – a product of combustion, as well as molten deposits resulting from siliceous debris ingested into engines. $RE_2O_3$ are a class of oxides that are relatively impervious to reaction with high temperature high-velocity steam. $Y_2O_3$ exposed to 1 atm steam at 1400 °C for 60 h, with a steam velocity of 225 m/s showed no recession within a sensitivity of 2 μm [56]. For comparison, $Al_2O_3$ undergoes 80 μm recession due to $Al(OH)_3$(g) formation at 1400 °C after 48 h under the same high-velocity steam conditions [57].

**Siliceous Debris Exposure Stability:** $RE_2O_3$ are also comparatively stable to dissolution in molten siliceous debris ($CaO{\cdot}MgO{\cdot}Al_2O_3{\cdot}SiO_2$ – CMAS) relative to $RE_2Si_2O_7$ EBCs for SiC-based composite substrates [58]. Few studies exist for $RE_2O_3$ – CMAS interactions [59,60], and only at temperatures of 1350 °C and lower, for times of 10 h or less. Fig. 4(a) shows a scanning electron microscopy (SEM) cross-sectional image and Fig. 4(b) the energy dispersive spectroscopy (EDS) elemental maps of a five component MRO material $(Y_{0.2}Yb_{0.2}Er_{0.2}Ho_{0.2}Nd_{0.2})_2O_3$ after reaction with CMAS at 1500 °C, for 100 h in air, much more severe conditions than typically studied. The CMAS viscosity at 1500 °C was sufficiently low that the CMAS wet and spread over the coupon surface uniformly reacting to form a protective barrier layer of reaction product composed of Ca-stabilized apatite $Ca_2RE_8(SiO_4)_6O_2$ and cuspidine $(Ca,RE)_4(Al,Si)_2O_9$ the mineral name for Ca and Si-substituted YAM (Yttrium Aluminum Monoclinic). The reaction product layer shown at high magnification in Fig. 4**(a)** was uniform across the underlying MRO, showing an initial transient of product formation and 20 μm of substrate recession in 1 h, followed by minimal additional recession as measured up to 24 h. Here, the selection of RE components in the MRO composition is critical to control the barrier product phase, demonstrating the possibility of optimizing CMAS resistance through a selection of appropriate $RE_2O_3$. Large RE cations, such as Nd, are strongly favored in the apatite phase [61]. Furthermore, multiple cations were added into a single solution for thermochemical stability and succeeded without losing other desirable MRO properties (i.e., isotropic crystallographic structure), as seen in Fig. 4**(c),(d)**.

A major challenge for predicting CMAS reactions with MRO compositions based on CALPHAD approach is the lack of thermodynamic data of the apatite and cuspidine phases for various REs. To analyze the equilibrium reaction products and their compositions, a thermodynamic database was developed for apatite ($Ca_2RE_8(SiO_4)_6O_2$), cuspidine (or YAM, $(Ca,RE)_4(Al,Si)_2O_9$) and monosilicates ($RE_2SiO_5$) as oxide solution phases with multiple relevant REs. The formation energies of the end-members are from published experiments or current calculations density functional theory (DFT) [62,63]. The mixing energies of REs on the cation sublattices were calculated by DFT with the disordered structures mimicked by the special quasi-random structures [64]. For the reaction between the five component MRO and CMAS, the calculated equilibrium phases and their compositions with the developed CALPHAD database generally agree with the experiment (Fig. 4**(a), (b)**), with the apatite being Nd-rich while the cuspidine being Yb-rich.

### *Oxygen and RE diffusion in MRO compositions*

The prime function of a MRO coating is to limit oxidant access from the combustion gases to the underlying refractory alloy. Relatively few data exist for oxygen self-diffusion in $RE_2O_3$ to enable evaluation of the intrinsic barrier capabilities of these materials. In one study, an oxygen diffusivity of $10^{-11}$ $cm^2/s$ (1400 °C) is reported for single crystal cubic $Y_2O_3$ obtained over the temperature range 1100–1500 °C via the tracer method [65]. RE cation diffusion is also important for densification of coatings deposited by atmospheric plasma spray or slurry processing. Since little to no experimental data exist, a computational assessment of periodic trends was undertaken to examine the rates of diffusion, the migration barriers of $O^{2-}$ anion and $RE^{3+}$ cations in cubic $RE_2O_3$ using DFT in combination with the climbing image nudged elastic band method [66]. The magnetic states of the RE ions cause difficulties in structural relaxations with DFT, which will be described in a separate publication. As shown in Fig. 5, both the migration barriers for $O^{2-}$ (a) and $RE^{3+}$ (b) in $RE_2O_3$ with lanthanides generally decrease with increasing effective ionic radius. Therefore, REs with smaller radii should be prioritized to mitigate oxygen diffusion, while REs with larger radii should be prioritized for better densification. The major challenge for implementing MRO coatings as oxygen diffusion barriers for RMAs in aeroturbine engines is the necessity for full density, defect free coatings

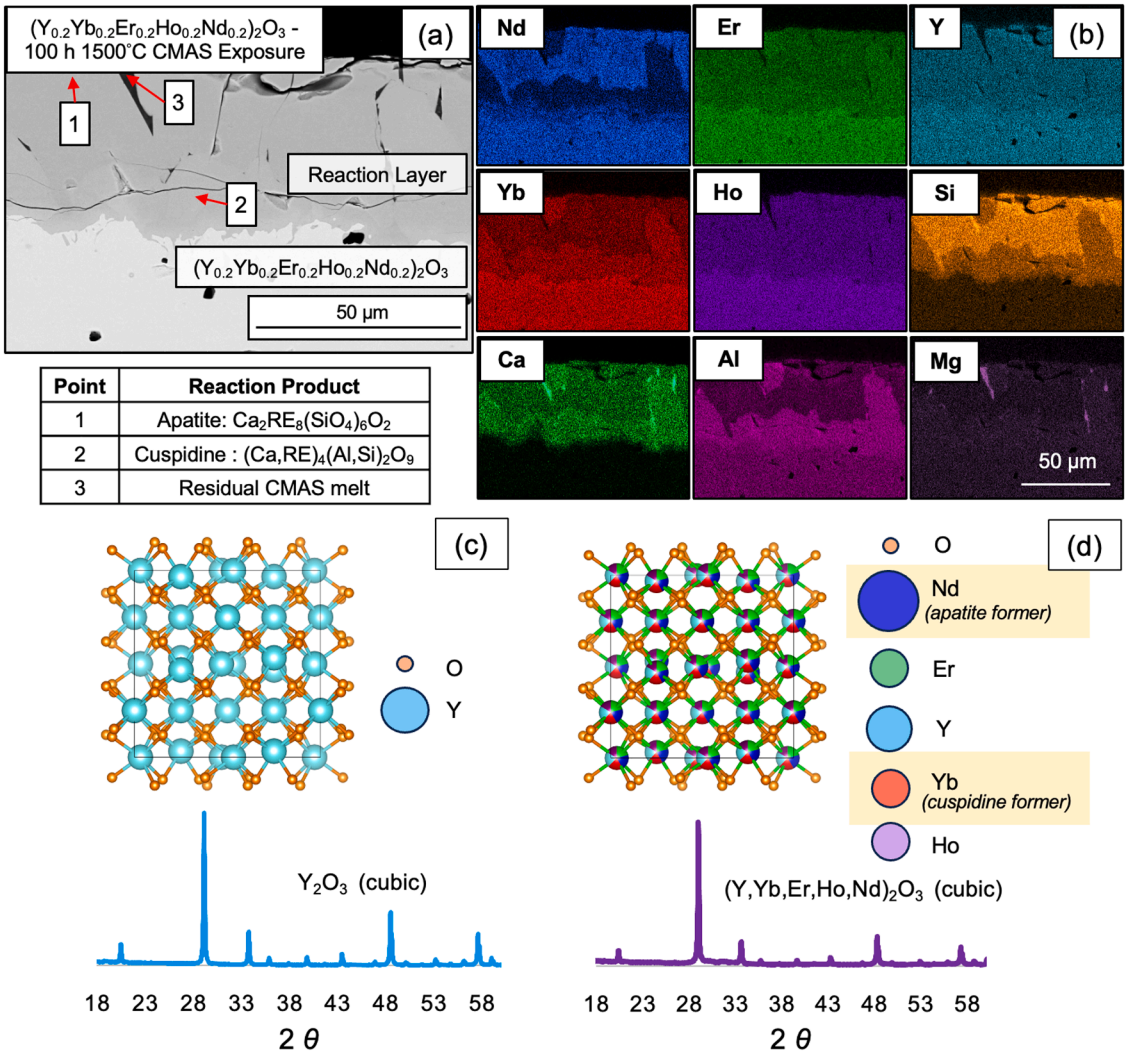


**Fig. 4.** (a) SEM cross-sectional image of five component MRO $(Y_{0.2}Yb_{0.2}Er_{0.2}Ho_{0.2}Nd_{0.2})_2O_3$ after exposure to 20 mg/cm$^2$ of CMAS (33 CaO–9 MgO–13$AlO_{1.5}$–45$SiO_2$ mol%) at 1500 °C for 100 h in air with (b) corresponding EDS maps. Note the preferential inclusion of Nd in the apatite phase and Yb in the cuspidine phase;(c) Single component $Y_2O_3$ cubic crystal structure with no strong CMAS reaction layer formers; (d) Five component MRO composition $(Y_{0.2}Yb_{0.2}Er_{0.2}Ho_{0.2}Nd_{0.2})_2O_3$ cubic crystal structure with Nd apatite former and Yb cuspidine/garnet former.

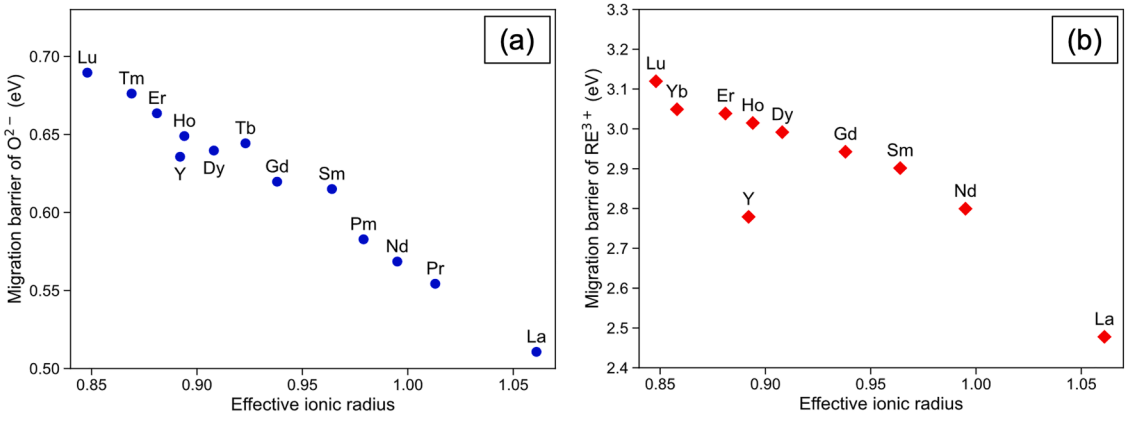


**Fig. 5.** The migration barrier of $O^{2-}$ (a) and $RE^{3+}$ (b) in cubic $RE_2O_3$ from DFT calculations as functions of the effective ionic radii.

in the as-synthesized state, as well as an understanding of transport in grain or splat boundaries. This is an unexplored area for applications where dense coatings are desired.

*Outlook*

Refractory metals suffer from poor oxidation resistance in high temperature reactive environments such as hot sections of turbine

engines. Here we propose that compositional control of multicomponent rare earth oxides (MROs) enables co-optimization of multiple required coating properties including thermal expansion, thermal conductivity, radiative absorption, stability in high temperature steam-containing combustion environments, stability toward molten deposits, and tailorability of both cation and anion diffusivities. Computational thermodynamics (DFT and CALPHAD) and machine learning are needed to explore compositional space in the absence of significant experimental data. Proof-of-concept niobium alloy (C-103)/MRO coating systems have demonstrated feasibility of coating synthesis by atmospheric plasma spray and hybrid slurry coating fabrication approaches. Challenges and remaining unexplored issues for success of refractory metal/MRO high temperature material systems have been identified.

## CRediT authorship contribution statement

**Kristyn D. Ardrey:** Writing – review & editing, Writing – original draft, Methodology, Investigation, Formal analysis, Data curation, Conceptualization. **Mackenzie J. Ridley:** Investigation, Formal analysis, Data curation. **Kang Wang:** Software, Methodology, Investigation, Data curation, Conceptualization. **Kevin Reuwer:** Methodology, Investigation, Formal analysis, Data curation. **Giavanna Angelo:** Investigation, Formal analysis, Data curation. **Kevin Childrey:** Formal analysis, Data curation. **William Riffe:** Formal analysis, Data curation. **Mahboobe Jassas:** Formal analysis, Data curation. **Mukil Ayyasamy:** Formal analysis, Data curation. **Prasanna V. Balachandran:** Writing – original draft, Visualization, Validation, Supervision, Software, Project administration, Methodology, Investigation, Formal analysis, Conceptualization. **Patrick E. Hopkins:** Writing – review & editing, Writing – original draft, Visualization, Validation, Supervision, Project administration, Methodology, Investigation, Formal analysis, Data curation, Conceptualization. **Jonathan Laurer:** Writing – original draft, Supervision, Investigation, Formal analysis, Data curation, Conceptualization. **Carolina Tallon:** Writing – original draft, Supervision, Conceptualization, Formal analysis, Data curation. **Bi-Cheng Zhou:** Writing – original draft, Supervision, Software, Project administration, Methodology, Investigation, Formal analysis, Data curation, Conceptualization. **Elizabeth J. Opila:** Writing – review & editing, Writing – original draft, Validation, Supervision, Investigation, Formal analysis, Conceptualization.

## Declaration of competing interest

The authors declare the following financial interests/personal relationships which may be considered as potential competing interests: Patent application filed for presented technology in manuscript.

## Acknowledgments

The authors gratefully acknowledge helpful discussions with Dr. Robert Golden, Rolls-Royce Corporation, use of the University of Virginia Nanoscale Characterization Facility, funding from the US Department of Energy, award number DE-AR0001425 under the ARPA-E ULTIMATE program, and support from the Office of Naval Research, grant number N00014-21-1-2477.

## References

[1] B.P. Bewlay, M.R. Jackson, P.R. Subramanian, J.C. Zhao, A review of very-high-temperature Nb-silicide-based composites, Metall. Mater. Trans. A 34 (2003) 2043–2052.
[2] M.D. Novak, C.G. Levi, Oxidation and volatilization of silicide coatings for refractory niobium alloys, in: Advances in aerospace technology, 1, ASMEDC, Seattle, Washington, USA, 2007, pp. 261–267.
[3] B.T. Richards, M.R. Begley, H.N.G. Wadley, Mechanisms of ytterbium monosilicate/mullite/silicon coating failure during thermal cycling in water vapor, J. Am. Ceram. Soc. 98 (2015) 4066–4075.
[4] R. Braun, A. Lange, U. Schulz, L. Portebois, S. Mathieu, M. Vilasi, S. Drawin, Lifetime of environmental/thermal barrier coatings deposited on a niobium silicide composite with boron containing $M_7Si_6$-based bond coat, Mater. Corros. 67 (2016) 1252–1260.
[5] S.S. Panwar, T.U. Patro, K. Balasubramanian, B. Venkataraman, High-temperature stability of yttria-stabilized zirconia thermal barrier coating on niobium alloy—C-103, Bull Mater Sci 39 (2016) 321–329.
[6] R.A. Golden, K. Mueller, E.J. Opila, Thermochemical stability of $Y_2Si_2O_7$ in high-temperature water vapor, J. Am. Ceram. Soc. 103 (2020) 4517–4535.
[7] E.J. Opila, J.L. Smialek, R.C. Robinson, D.S. Fox, N.S. Jacobson, SiC recession caused by $SiO_2$ scale volatility under combustion conditions: II, thermodynamics and gaseous-diffusion model, J. Am. Ceram. Soc. 82 (1999) 1826–1834.
[8] P. Mechnich, W. Braue, Air plasma-sprayed $Y_2O_3$ coatings for $Al_2O_3/Al_2O_3$ ceramic matrix composites, J. Eur Ceram Soc. 33 (2013) 2645–2653.
[9] B. Abeles, Lattice thermal conductivity of disordered semiconductor alloys at high temperatures, Phys. Rev. 131 (1963) 1906.
[10] M. Ridley, J. Gaskins, P. Hopkins, E. Opila, Tailoring thermal properties of multi-component Rare Earth monosilicates, Acta Mater 195 (2020) 698–707.
[11] C. Toher, M. Ridley, K. Tomko, D. Olson, S. Curtarolo, P. Hopkins, E. Opila, Design rules for the thermal and elastic properties of rare-earth disilicates, Materialia 28 (2023) 101729.
[12] M. Chen, B. Hallstedt, L.J. Gauckler, CALPHAD modeling of the $La_2O_3$–$Y_2O_3$ system, CALPHAD. 29 (2005) 103–113.
[13] M. Zinkevich, Thermodynamics of rare earth sesquioxides, Prog Mater Sci. 52 (2007) 597–647.
[14] P.V. Balachandran, Adaptive machine learning for efficient materials design, MRS Bull. 45 (2020) 579–586.
[15] M. Pistilli, Rare earth elements prices 101 (updated 2024), INN (2024). URL, https://investingnews.com/daily/resource-investing/critical-metals-investing/rare-earth-investing/rare-earth-metals-prices/ (accessed 5.15.24).
[16] M.X. Zhang, Y.A. Chang, Phase diagrams of Ti-AL-C, Ti-Y-O, Nb-Y-O, and Nb-Al-O at 1100 °C, JPE 15 (1994) 470–472.
[17] M. Challarapu, Surry based coatings on silicon based ceramics, Cleveland State University, 2009.
[18] S.K. Khaja-Abdul, Slurry based coatings on silicon based ceramics, Cleveland State University, 2008.
[19] S. Ramasamy, S.N. Tewari, K.N. Lee, R.T. Bhatt, D.S. Fox, EBC development for hot-pressed $Y_2O_3/Al_2O_3$ doped silicon nitride ceramics, Mater. Sci. Eng. 527 (2010) 5492–5498.
[20] S. Ramasamy, S.N. Tewari, K.N. Lee, R.T. Bhatt, D.S. Fox, Slurry based multilayer environmental barrier coatings for silicon carbide and silicon nitride ceramics—I. Processing, Surface Coat. Techn. 205 (2010) 258–265.
[21] S. Ramasamy, S.N. Tewari, K.N. Lee, R.T. Bhatt, D.S. Fox, Slurry based multilayer environmental barrier coatings for silicon carbide and silicon nitride ceramics—II. Oxidation resistance, Surface Coat. Techn. 205 (2010) 266–270.
[22] S. Ramasamy, S.N. Tewari, K.N. Lee, R.T. Bhatt, D.S. Fox, Mullite–gadolinium silicate environmental barrier coatings for melt infiltrated SiC/SiC composites, Surface Coat. Techn. 205 (2011) 3578–3581.
[23] Z. Hong, L. Cheng, L. Zhang, Y. Wang, Internal friction behavior of C/SiC composites with environmental barrier coatings in corrosive environment, Int. J. Appl. Ceram. Technol. 8 (2011) 342–350.
[24] T. Suetsuna, T. Ohji, Oxidation of silicon nitride in wet air and effect of lutetium disilicate coating, J. Am. Ceramic Soc. 88 (2005) 1139–1144.
[25] M.D. Nguyen, J.W. Bang, Y.H. Kim, A.S. Bin, K.H. Hwang, V.H. Pham, W.T. Kwon, Slurry spray coating of carbon steel for use in oxidizing and humid environments, Ceram Int 44 (2018) 8306–8313.
[26] X. Shan, L.Q. Wei, X.M. Zhang, W.H. Li, W.X. Tang, Y. Liu, J. Tong, S.F. Ye, Y. F. Chen, A protective ceramic coating to improve oxidation and thermal shock resistance on CrMn alloy at elevated temperatures, Ceram Int 41 (2015) 4706–4713.
[27] G.V. Franks, C. Tallon, A.R. Studart, M.L. Sesso, S. Leo, Colloidal processing: enabling complex shaped ceramics with unique multiscale structures, J. Am. Ceramic Soc. 100 (2017) 458–490.
[28] S.C. Santos, W. Acchar, C. Yamagata, S. Mello-Castanho, Yttria nettings by colloidal processing, J. Eur. Ceram Soc. 34 (2014) 2509–2517.
[29] C.C. Wojcik, Thermomechanical processing and properties of niobium alloys, niobium, Sci. Technol. (2001) 163–173.
[30] Y.C. Yu, D.L. Poerschke, Design of thermal and environmental barrier coatings for Nb-based alloys for high-temperature operation, Surface Coat. Techn. 431 (2022) 128007.
[31] O.N. Senkov, J.M. Scott, S.V. Senkova, D.B. Miracle, C.F. Woodward, Microstructure and room temperature properties of a high-entropy TaNbHfZrTi alloy, J. Alloys Compd. 509 (2011) 6043–6048.
[32] D.R. Clarke, M. Oechsner, N.P. Padture, Thermal-barrier coatings for more efficient gas-turbine engines, MRS Bull. 37 (2012) 891–898.
[33] R. Banerjee, S. Chatterjee, M. Ranjan, T. Bhattacharya, S. Mukherjee, S.S. Jana, A. Dwivedi, T. Maiti, High-entropy perovskites: an emergent class of oxide thermoelectrics with ultralow thermal conductivity, ACS Sustain. Chem. Eng 8 (2020) 17022–17032.
[34] J.L. Braun, C.M. Rost, M. Lim, A. Giri, D.H. Olson, G.N. Kotsonis, G. Stan, D. W. Brenner, J. Maria, P.E. Hopkins, Charge-induced disorder controls the thermal conductivity of entropy-stabilized oxides, Adv. Mater. 30 (2018) 1805004.
[35] M. Lim, Z. Rak, J. Braun, C. Rost, G. Kotsonis, P. Hopkins, J.P. Maria, D. Brenner, Influence of mass and charge disorder on the phonon thermal conductivity of entropy stabilized oxides determined by molecular dynamics simulations, J. Appl. Phys 125 (2019).

[36] C.M. Rost, E. Sachet, T. Borman, A. Moballegh, E.C. Dickey, D. Hou, J.L. Jones, S. Curtarolo, J.P. Maria, Entropy-stabilized oxides, Nat Commun. 6 (2015) 8485.
[37] C.M. Rost, D.L. Schmuckler, C. Bumgardner, M.S. Bin Hoque, D.R. Diercks, J. T. Gaskins, J.P. Maria, G.L. Brennecka, X. Li, P.E. Hopkins, On the thermal and mechanical properties of $Mg_{0.2}Co_{0.2}Ni_{0.2}Cu_{0.2}Zn_{0.2}O$ across the high-entropy to entropy-stabilized transition, APL Mater 10 (2022).
[38] Y. Sharma, B.L. Musico, X. Gao, C. Hua, A.F. May, A. Herklotz, A. Rastogi, D. Mandrus, J. Yan, H.N. Lee, Single-crystal high entropy perovskite oxide epitaxial films, Phys. Rev. Mater. 2 (2018) 060404.
[39] D.G. Cahill, S.K. Watson, R.O. Pohl, Lower limit to the thermal conductivity of disordered crystals, Phys. Rev. B 46 (1992) 6131.
[40] L.R. Turcer, A. Sengupta, N.P. Padture, Low thermal conductivity in high-entropy rare-earth pyrosilicate solid-solutions for thermal environmental barrier coatings, Scr Mater 191 (2021) 40–45.
[41] M. Ridley, J. Gaskins, P. Hopkins, E. Opila, Tailoring thermal properties of multi-component rare earth monosilicates, Acta Mater 195 (2020) 698–707.
[42] A. Giri, J.L. Braun, C.M. Rost, P.E. Hopkins, On the minimum limit to thermal conductivity of multi-atom component crystalline solid solutions based on impurity mass scattering, Scr. Mater 138 (2017) 134–138.
[43] P.H. Klein, W.J. Croft, Thermal conductivity, diffusivity, and expansion of $Y_2O_3$, $Y_3Al_5O_{12}$, and $LaF_3$ in the range 77–300 K, J Appl Phys 38 (1967) 1603–1607.
[44] P.H. Klein, Thermal conductivity, thermal diffusivity, and specific heat of solids from a single experiment, with application to $Y_{1.98}Nd_{0.02}O_3$, J Appl Phys 38 (1967) 1598–1603.
[45] D.G. Cahill, P.V. Braun, G. Chen, D.R. Clarke, S. Fan, K.E. Goodson, P. Keblinski, W. P. King, G.D. Mahan, A. Majumdar, H.J. Maris, S.R. Phillpot, E. Pop, L. Shi, Nanoscale thermal transport. II. 2003–2012, Appl. Phys. Rev. 1 (2014) 011305.
[46] D.G. Cahill, Analysis of heat flow in layered structures for time-domain thermoreflectance, Rev. Scient. Instrum. 75 (2004) 5119–5122.
[47] A.J. Schmidt, Pump-probe thermoreflectance, Annual Rev. Heat Transfer 16 (2013).
[48] A.J. Schmidt, X. Chen, G. Chen, Pulse accumulation, radial heat conduction, and anisotropic thermal conductivity in pump-probe transient thermoreflectance, Rev. Scient. Instrum. 79 (2008).
[49] D.H. Olson, V.A. Avincola, C.G. Parker, J.L. Braun, J.T. Gaskins, J.A. Tomko, E. J. Opila, P.E. Hopkins, Anisotropic thermal conductivity tensor of $\beta$-$Y_2Si_2O_7$ for orientational control of heat flow on micrometer scales, Acta Mater 189 (2020) 299–305.
[50] D.H. Olson, J.T. Gaskins, J.A. Tomko, E.J. Opila, R.A. Golden, G.J. Harrington, A. L. Chamberlain, P.E. Hopkins, Local thermal conductivity measurements to determine the fraction of α-cristobalite in thermally grown oxides for aerospace applications, Scr Mater 177 (2020) 214–217.
[51] D.H. Olson, J.A. Deijkers, K. Quiambao-Tomko, J.T. Gaskins, B.T. Richards, E. J. Opila, P.E. Hopkins, H.N. Wadley, Evolution of microstructure and thermal conductivity of multifunctional environmental barrier coating systems, Mater. Today Phys. 17 (2021) 100304.
[52] X. Zheng, D.G. Cahill, J. Zhao, Thermal conductivity imaging of thermal barrier coatings, Adv. Eng Mater 7 (2005) 622–626.
[53] D.H. Olson, J.L. Braun, P.E. Hopkins, Spatially resolved thermoreflectance techniques for thermal conductivity measurements from the nanoscale to the mesoscale, J Appl. Phys 126 (2019).
[54] Q. Flamant, D.R. Clarke, Opportunities for minimizing radiative heat transfer in future thermal and environmental barrier coatings, Scr. Mater 173 (2019) 26–31.
[55] G.E. Guazzoni, High-temperature spectral emittance of oxides of erbium, samarium, neodymium and ytterbium, Appl. Spectrosc 26 (1972) 60–65.
[56] C.G. Parker, E.J. Opila, Stability of the $Y_2O_3$–$SiO_2$ system in high-temperature, high-velocity water vapor, J. Am. Ceramic Soc. 103 (2020) 2715–2726.
[57] M.J. Ridley, E.J. Opila, Quantitative evaluation of (0001) sapphire recession in high-temperature high-velocity steamjet exposures, J. Eur. Ceram Soc. 42 (2022) 631–637.
[58] R.I. Webster, E.J. Opila, Mixed phase ytterbium silicate environmental-barrier coating materials for improved calcium–magnesium–alumino-silicate resistance, J. Mater Res 35 (2020) 2358–2372.
[59] L. Guo, B. Zhang, Y. Gao, K. Yan, Interaction laws of $RE_2O_3$ and CMAS and rare earth selection criterions for RE-containing thermal barrier coatings against CMAS attack, Corros Sci. 226 (2024) 111689.
[60] Y. Sun, H. Xiang, F.Z. Dai, X. Wang, Y. Xing, X. Zhao, Y. Zhou, Preparation and properties of CMAS resistant bixbyite structured high-entropy oxides $RE_2O_3$ (RE = Sm, Eu, Er, Lu, Y, and Yb): promising environmental barrier coating materials for Al2O3f/Al2O3 composites,, J. Adv. Ceram 10 (2021) 596–613.
[61] G. Costa, B.J. Harder, N.P. Bansal, B.A. Kowalski, J.L. Stokes, Thermochemistry of calcium rare-earth silicate oxyapatites, J. Am. Ceramic Soc. 103 (2020) 1446–1453.
[62] W. Kohn, L. Sham, Self-consistent equations including exchange and correlation effects, Phys. Rev.A 140 (1965) 1133.
[63] P. Hohenberg, W. Kohn, Density functional theory (DFT), Phys. Rev. B (1964) 864.
[64] A. Zunger, S.H. Wei, L.G. Ferreira, J.E. Bernard, Special quasirandom structures, Phys. Rev. Lett. 65 (1990) 353.
[65] K. Ando, Y. Oishi, H. Hase, K. Kitazawa, Oxygen self-diffusion in single-crystal $Y_2O_3$, J. Am. Ceramic Soc. 66 (1983). C-222-C–223.
[66] G. Henkelman, B.P. Uberuaga, H. Jónsson, A climbing image nudged elastic band method for finding saddle points and minimum energy paths, J. Chem. Phys 113 (2000) 9901–9904.